Cell, Vol. 121, 1043–1057, July 1, 2005, Copyright ©2005 by Elsevier Inc. DOI 10.1016/j.cell.2005.05.025

Crystal Structure of Mitochondrial Respiratory Membrane Protein Complex II

Fei Sun,[1,2] Xia Huo,[2] Yujia Zhai,[1] Aojin Wang,[2] Jianxing Xu,[2] Dan Su,[1] Mark Bartlam,[1,2] and Zihe Rao[1,2,*]

[1]Tsinghua-IBP Joint Research Group for Structural Biology
Tsinghua University
Beijing 100084
China

[2]National Laboratory of Biomacromolecules
Institute of Biophysics (IBP)
Chinese Academy of Sciences
Beijing 100101
China

Summary

The mitochondrial respiratory Complex II or succinate: ubiquinone oxidoreductase (SQR) is an integral membrane protein complex in both the tricarboxylic acid cycle and aerobic respiration. Here we report the first crystal structure of Complex II from porcine heart at 2.4 Å resolution and its complex structure with inhibitors 3-nitropropionate and 2-thenoyltrifluoroacetone (TTFA) at 3.5 Å resolution. Complex II is comprised of two hydrophilic proteins, flavoprotein (Fp) and iron-sulfur protein (Ip), and two transmembrane proteins (CybL and CybS), as well as prosthetic groups required for electron transfer from succinate to ubiquinone. The structure correlates the protein environments around prosthetic groups with their unique midpoint redox potentials. Two ubiquinone binding sites are discussed and elucidated by TTFA binding. The Complex II structure provides a bona fide model for study of the mitochondrial respiratory system and human mitochondrial diseases related to mutations in this complex.

Introduction

Mitochondria are cellular organelles of prokaryotic origin that are found in almost all eukaryotic cells. The mitochondrial respiratory system, consisting of five membrane protein complexes (I to V), produces most of the energy in eukaryotic cells (Saraste, 1999). To date, the structures of Complex III (cytochrome bc_1 complex) (Iwata et al., 1998; Lange and Hunte, 2002; Xia et al., 1997; Zhang et al., 1998), Complex IV (cytochrome c oxidase complex) (Tsukihara et al., 1995; Tsukihara et al., 1996), and Complex V (ATPase) (Abrahams et al., 1994) have been determined. However, no breakthroughs have been made on the structures of complexes I and II.

Mitochondrial Complex II, also known as mitochondrial succinate:ubiquinone oxidoreductase (mitochondrial SQR) (EC 1.3.5.1), is a key membrane complex in the Krebs cycle (tricarboxylic acid cycle) that catalyzes the oxidation of succinate to fumarate in the mitochondrial matrix as succinate dehydrogenase. Succinate oxidation is coupled to reduction of ubiquinone to ubiquinol at the mitochondrial inner membrane as one part of the respiration electron transfer chain (Figure 1). Electrons are transferred from succinate to ubiquinone through the buried prosthetic groups flavin-adenine dinucleotide (FAD); the [2Fe-2S], [4Fe-4S], and [3Fe-4S] clusters; and heme, which form an integral part of the complex (Hagerhall, 1997).

Succinate:ubiquinone oxidoreductase normally consists of a soluble catalytic heterodimer and an integral membrane region. The soluble catalytic heterodimer is made up of subunit A with a covalently bound FAD cofactor and subunit B containing three iron-sulfur clusters: [2Fe-2S], [4Fe-4S], and [3Fe-4S] (Hagerhall, 1997). The integral membrane region anchoring the complex to the inner membrane contains one or two hydrophobic peptides with or without heme groups. Succinate: ubiquinone oxidoreductases can be classified into five types (A–E) according to the number of their hydrophobic subunits and heme groups (Lemos et al., 2002). The mitochondrial SQRs belong to type C and contain one heme molecule and two transmembrane proteins: the large cytochrome b binding protein (CybL or subunit C) and the small cytochrome b binding protein (CybS or subunit D) (Lemos et al., 2002). To date, only the structures of prokaryotic succinate:ubiquinone oxidoreductases (one for type B, one for type D, and one for type C), which share a similar enzymatic function with mitochondrial SQR (Complex II), have been reported (Iverson et al., 1999; Lancaster et al., 1999; Yankovskaya et al., 2003).

Today, important questions remain on the mechanism of ubiquinone reduction by Complex II and the process for ubiquinone transition between Complex II and Complex III. Probing the location and number of ubiquinone reaction sites in mitochondrial Complex II is therefore essential to address the above questions. In the absence of a reliable three-dimensional structure of mitochondrial SQR (Complex II), researchers often used prokaryotic SQR and quinone:fumarate reductase (QFR) structures (Iverson et al., 1999; Lancaster et al., 1999; Yankovskaya et al., 2003) as models to investigate the ubiquinone binding sites. However, questions still remain for two reasons. First, the sequence homology of the integral membrane anchors between mitochondrial SQR (Complex II) and prokaryotic SQR is less than 20% (Figures 2A and 2B), indicating that the hydrophobic domains undergo unique evolutionary pressure imposed by different functions. Secondly, ubiquinone analog inhibitors such as 2-thenoyltrifluoroacetone (TTFA) and carboxanilide (carboxin), which are vital for studying mitochondrial Complex II quinone-reduction activity and its Q pool, only weakly inhibit their bacterial counterparts (Maklashina and Cecchini, 1999; Yankovskaya et al., 1996). This observation strongly suggests that mitochondrial Complex II has ubiquinone binding pockets (conformations and/or positions) different from those of its prokaryotic counterparts.

*Correspondence: raozh@xtal.tsinghua.edu.cn

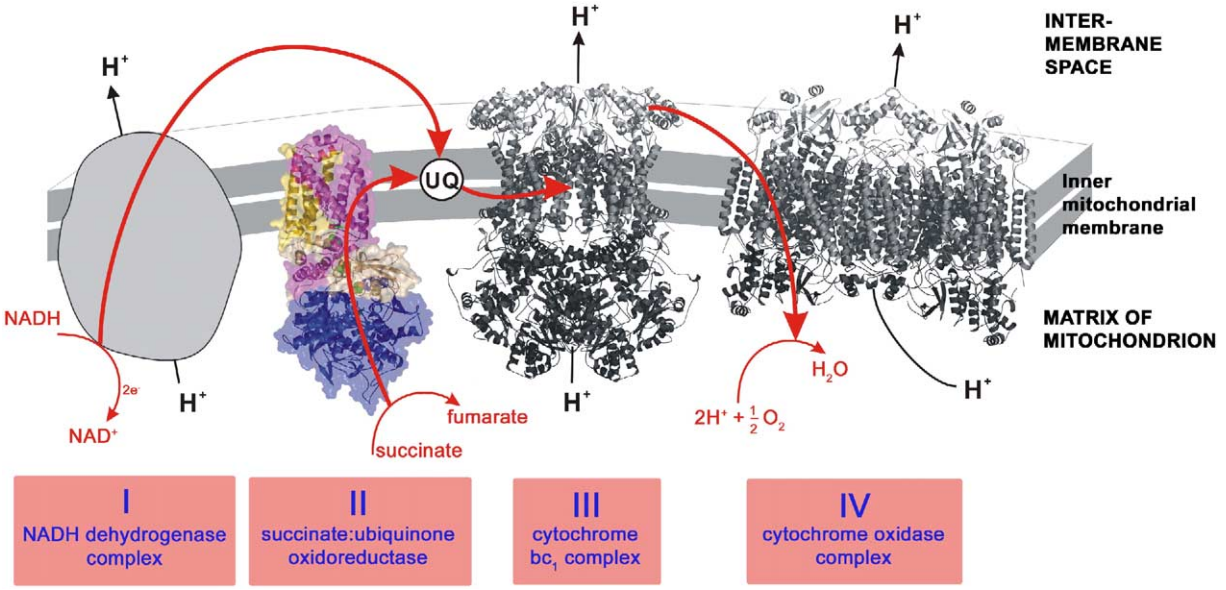

Figure 1. The Role of Complex II in the Mitochondrial Respiratory Chain

The relative size and shape of mitochondrial Complex II–IV, as well as a schematic of Complex I, are shown. The transfer of electrons is shown by red lines. Mitochondrial Complex II couples the Krebs cycle with the electron transfer chain comprised of Complex I, Complex III (Iwata et al., 1998), and Complex IV (Tsukihara et al., 1996). UQ indicates ubiquinone, which serves as a mobile carrier to transport electrons from Complex I or II to Complex III.

Inactivation of mitochondrial Complex II either by premature termination or by mutation has manifested a range of diseases such as familial pheochromocytoma, familial head-and-neck paraganglioma, and Leigh syndrome (Ackrell, 2002; Astuti et al., 2001a; Astuti et al., 2001b; Baysal et al., 2000; Bourgeron et al., 1995; Douwes Dekker et al., 2003; Ishii et al., 1998; Niemann and Muller, 2000; Rustin and Rotig, 2002). These diseases often demonstrate neurological disorders and are mainly related with production of reactive oxygen species (ROS) (Rustin and Rotig, 2002). To date, attempts to integrate a wealth of data about these diseases have been hampered by the lack of a mitochondrial Complex II structure. Therefore, detailed structural information on mitochondrial Complex II is essential for functional, mechanistic, and clinical studies. Here, we report the first crystal structure of mitochondrial Complex II from porcine heart at 2.4 Å resolution and its complex structure with the inhibitors 3-nitropropionate (NPA) and 2-thenoyltrifluoroacetone (TTFA) at 3.5 Å resolution.

Results and Discussion

Structural Overview

The mitochondrial Complex II (124 kDa) was purified from porcine heart and crystallized in an orthorhombic crystal form (space group $P2_12_12_1$) with one complex per asymmetric unit. The structure contains four proteins: FAD binding protein or flavoprotein (Fp, 68 kDa, 622 amino acids), iron-sulfur protein (Ip, 29 kDa, 252 amino acids), and two membrane-anchor proteins (CybL, 15 kDa, 140 amino acids and CybS, 11 kDa, 103 amino acids) with a total of six transmembrane helices (Figure 3A). The data-collection, phase-calculation, and model-refinement statistics are summarized in Table 1.

The overall structure is shaped like the letter "q," with a hydrophilic head and a hydrophobic multipass transmembrane-anchor tail. The structure has a total surface area of 40,496 $Å^2$. As shown in Figure 3A, the hydrophilic head is 70 Å wide and 80 Å high, while the hydrophobic anchor tail has a width of ~45 Å and a height of ~45 Å. Approximately 40 Å of the anchor tail spans the transmembrane region, and five charged residues (Asp, Glu, and Lys) as well as two polar residues (Asn and Ser) are distributed around the bottom of the tail. We have assigned this complex as a transmembrane protein, i.e., the tail protrudes and is exposed into the intermembrane space.

The molecular packing in the crystal is partially mediated by interactions between neighboring transmembrane regions (see the Supplemental Data available with this article online). The packed transmembrane anchors form a thick membrane-like plane oriented at ~20° to the crystallographic c axis. The neighboring molecules orient in opposite directions with respect to the plane of the membrane domain, suggesting that the physiological form of the mitochondrial SQR is most likely to be a monomer, unlike that for *E. coli*, which is believed to be a trimer (Yankovskaya et al., 2003).

The Hydrophilic Head

The hydrophilic head of Complex II is comprised of subunit A, Fp, and subunit B, Ip. The N-terminal nine residues of Fp and the N-terminal eight and C-terminal

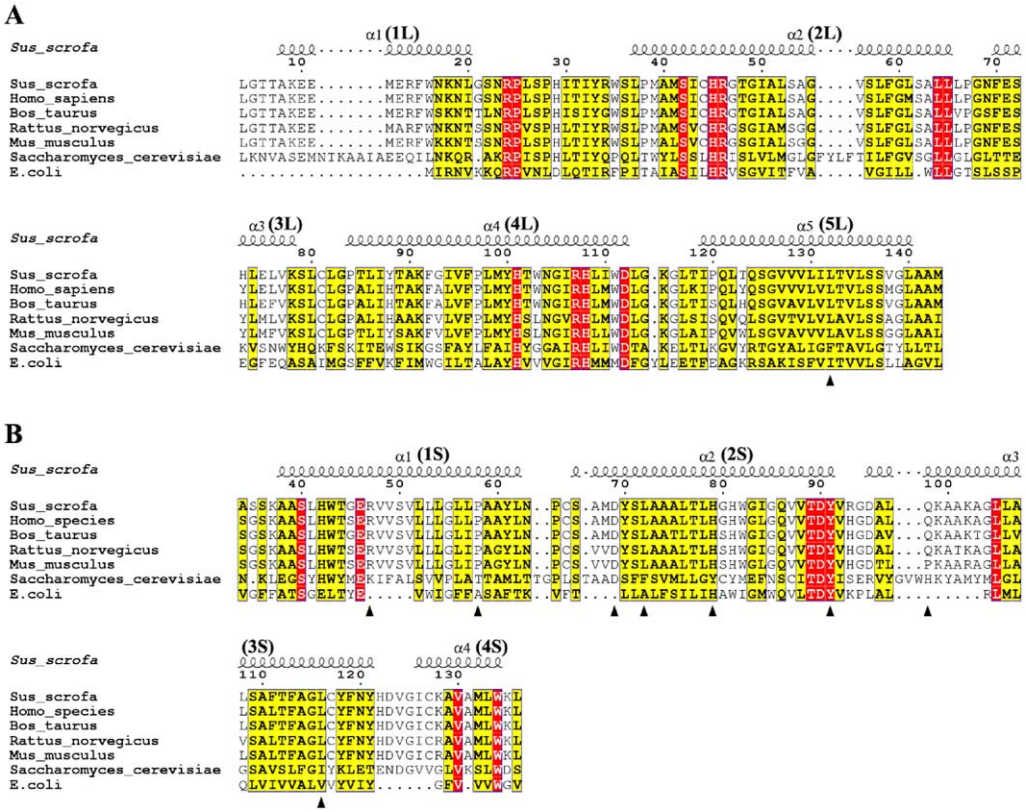

Figure 2. Multiple Alignment of SQR Sequences

(A) CybL (subunit C) and (B) CybS (subunit D). Sequences are shown for SQR from *Sus scrofa*, *Homo sapiens*, *Bos taurus*, *Rattus norvegicus*, *Mus musculus*, *Saccharomyces cerevisiae* and *E. coli*. Conserved residues are highlighted in red, and equivalent residues are highlighted in yellow. Secondary-structure elements are assigned according to the structure of porcine SQR. Residues related with mitochondrial diseases (Table 2) are marked by black triangles. The alignment was generated by ClustalW 1.7 (Thompson et al., 1994) and colored by ESPript (Gouet et al., 1999). Sequences representing signal peptides are not included in the alignment.

five residues of Ip were missing from the electron density map.

Fp has a Rossmann-type fold with four subdomains (Iverson et al., 1999; Lancaster et al., 1999; Yankovskaya et al., 2003): a large FAD binding domain (residues A10–A273 and A361–A445), a capping domain (A274–A360) with a βαβα structure, a helical domain (A446–A543) consisting of a single helix and a three-helix bundle, and a C-terminal domain (A554–A622) mainly consisting of one loop (A561–A579) and two β sheets (Figure 3B). The FAD binding domain can be divided into three parts: (1) an N-terminal β barrel subdomain (A10–A61 and A154–A273), (2) a floating subdomain (A62–A153) with two helices and seven small β strands, and (3) a subdomain (A361–A445) embedded between the above two domains. The core for FAD binding is composed of a ten-stranded, β sheet-like β barrel with three parallel helices on one side and one helix-like loop on the other (Figure 3B).

Ip, shaped like a butterfly, contains one N-terminal domain (B9–B114) with a main five-stranded β sheet and one small helix and one C-terminal α-helical domain (B115–B247) with six helices linked by loops (Figure 3B). The N-terminal domain contains a loop for [2Fe-2S] ligation, and the C-terminal domain is responsible for binding the [4Fe-4S] and [3Fe-4S] clusters.

The Hydrophobic Membrane Anchor

From the top view, the entire hydrophobic domain, containing two peptides, resembles a flower, with the heme group as its pistil and the transmembrane helices as leaves (Figure 3B). In this structure, CybL was traced for 138 residues with the N-terminal two residues missing, and CybS was traced for 102 residues with the N-terminal residue missing.

CybL has five helices (Figures 2A and 3B): helix 1L (C7–C21), helix 2L (C36–C66), helix 3L (C70–C80), helix 4L (C84–C114), and helix 5L (C119–C142); CybS has four helices (Figures 2B and 3B): helix 1S (D36–D62), helix 2S (D66–D92), helix 3S (D95–D123), and helix 4S (D126–D136). Both have a matrix-side N terminus and an intermembrane-space-side C terminus (Figures 3A and 3B). The N-terminal part of CybL forms a hydrophilic helix (helix 1L) that interacts with Ip. Transmembrane helices 2L and 4L of CybL and helices 1S and 2S of CybS are bound together and surrounded by helix 5L and helix 3S. The antiparallel helix 3L and helix 4S are arranged together near the intermembrane surface, making a closed structure below the four bundled helices (Figures 3A and 3B). These two antiparallel helices (3L and 4S) have a charged side emerging out of the membrane into the intermembrane space.

The angle (~50°) between helices 2L and 4L is large

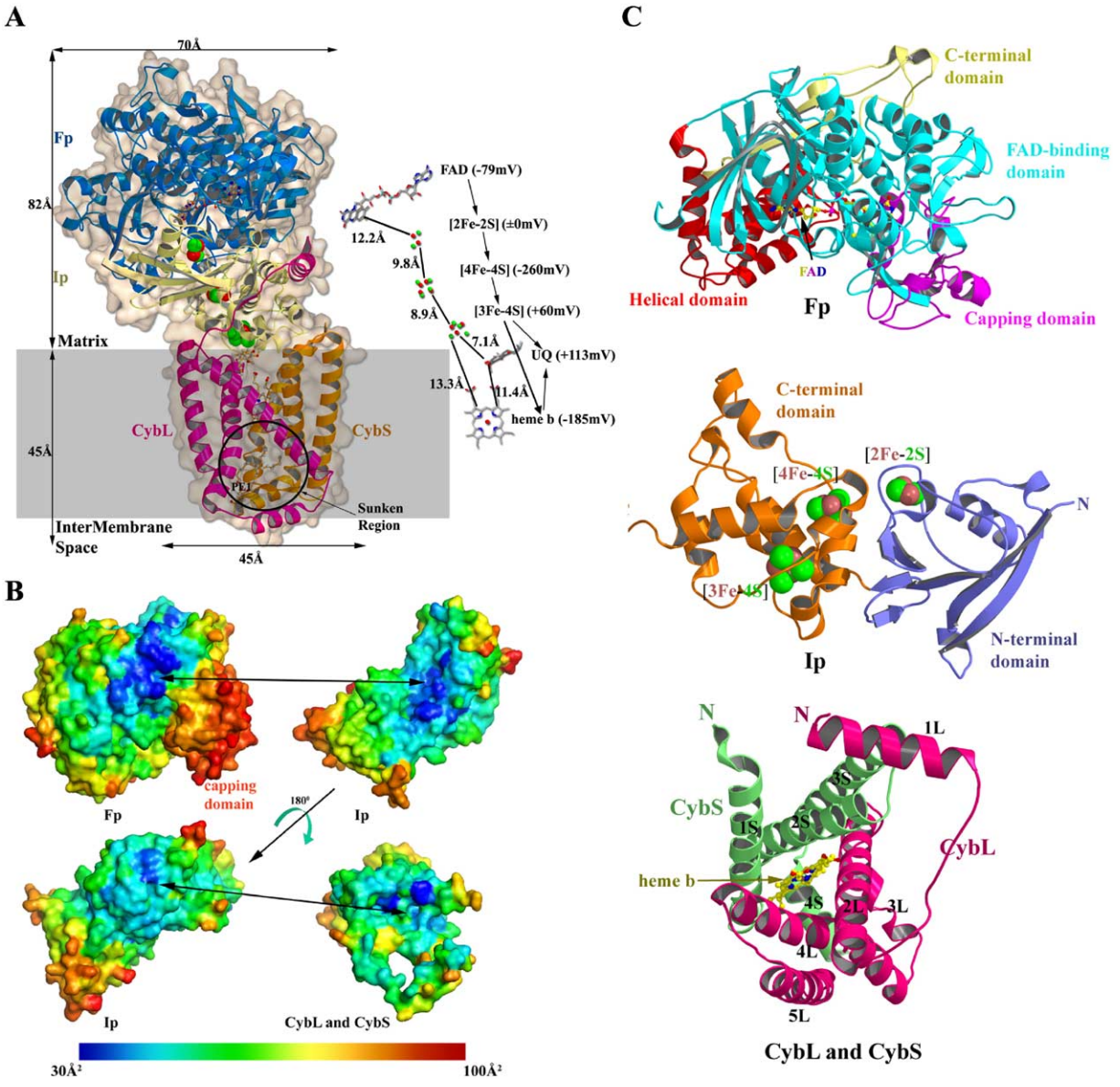

Figure 3. The Mitochondrial Respiratory Complex II Structure

(A) Overall structure of the mitochondrial respiratory Complex II, succinate:ubiquinone oxidoreductase (SQR). The ribbon diagram of the complex is superimposed on the semitransparent molecular surface. FAD binding protein (Fp) is shown in blue; iron-sulfur protein (Ip) is shown in cream; the transmembrane proteins CybL and CybS are shown in pink and gold, respectively. The putative membrane region is shaded in gray. On the right side, the prosthetic groups constituting the electron transfer pathway (FAD, [2Fe-2S], [4Fe-4S], [3Fe-4S], and heme b) are shown together with ubiquinone (UQ), along with their edge-to-edge distances and midpoint redox potentials (Hagerhall, 1997). The electron transfer flow at the Qp site is indicated by arrows. All figures were generated by BobScript (Esnouf, 1997).

(B) Description of subunits. Subunits of Fp, Ip, and the membrane anchor (CybL and CybS) are depicted in cartoon representation, with their respective prosthetic groups shown in ball-and-stick representation or as spheres. Unless otherwise specified, oxygen atoms are colored in red, nitrogen in blue, sulfur in green, phosphate in magenta, and iron in gold throughout all figures.

(C) Thermal-factor distribution around the contact surface. The temperature factors are shown mapped onto the molecular surface of Fp, Ip and transmembrane anchor. Temperature factors are colored from blue (30 Å^2) to red (100 Å^2). The contact surfaces between Fp and Ip and Ip and the transmembrane anchor are depicted by arrows. Temperature factors around the capping domain are quite high, indicating its flexibility, which could be caused by the lack of substrate-analog binding.

enough to endow an obvious sunken hydrophobic cavity below the heme group (Figure 3A). Four parallel aromatic residues, Tyr-C100, Phe-C96, Phe-C92, and Tyr-C88, are located at one side of helix 4L and form an ordered array from the matrix membrane side to the intermembrane side (see Supplemental Data). The center-to-center distances among these aromatic groups are all less than 7 Å. These groups should provide strong stacking interactions with each other and are beneficial for stability of the helix structure. These novel structural

Table 1. Data-Collection, SAD Phasing, and Refinement Statistics

Data-Collection Statistics			
Space group	$P2_12_12_1$		
Unit cell (Å)	a = 70.2 b = 83.6 c = 293.9		
	SAD	Native	Complex
Wavelength (Å)	1.74101	1.0322	0.9793
Resolution limit (Å)	50.0–3.0 (3.11–3.00)	50.0–2.4 (2.44–2.40)	50.0–3.5 (3.63–3.50)
Total reflections	150,760	546,106	93,526
Unique reflections	30,789	60,175	21,195
Completeness	85.9 (40.4)	85.1 (40.5)	93.9 (74.1)
R_{merge}[a]	10.3 (41.7)	12.5 (50.1)	7.8 (37.8)
$\langle I/\sigma(I)\rangle$	13.0 (2.0)	17.9 (2.9)	17.4 (3.2)
Redundancy	4.9 (4.5)	9.1 (3.6)	4.4 (3.5)
SAD Phasing Statistics			
Resolution range (Å)	50.0–3.5		
Figure of merit	0.19		
Phasing power	1.21		
R_{cullis}	0.78		
Refinement Statistics			
Resolution range (Å)	50.0–2.4	50.0–3.5	
R_{work}[b]	21.3	26.8	
R_{free}[b]	25.9	29.3	
RMS deviation			
Bonds (Å)	0.018	0.017	
Angles (°)	1.81	1.64	
Average B factors (Å^2)			
Protein (chain A/B/C/D)	69, 61, 71, 70	73, 71, 80, 80	
Water	69	40	

[a] $R_{merge} = \Sigma_h\Sigma_i|I_{ih} - \langle I_h\rangle|/\Sigma_h\Sigma_i\langle I_h\rangle$, where $\langle I_h\rangle$ is the mean of the observations I_{ih} of reflection h.
[b] $R_{work} = \Sigma(||F_p(obs)| - |F_p(calc)||)/\Sigma|F_p(obs)|$; R_{free} = R factor for a selected subset (5%) of the reflections that was not included in prior refinement calculations.

characteristics should be related to the function of Complex II and are suggested for future investigation.

Interactions between the Four Protein Subunits

The interactions between the four protein subunits of mitochondrial SQR are crucial for its formation, function, and stability. The contact-access surface area between Fp and Ip is about 2540 Å^2 in total, including 11.5% of the Fp surface area and 19.7% of the Ip surface area. The contact-access surface area between Ip and the transmembrane anchor is about 2320 Å^2, or 18% of the Ip surface area and 14.8% of the surface area of the transmembrane anchor. While there is no direct interaction between Fp and the hydrophobic membrane anchor, 40% of the total surface area of Ip contributes to the interaction with Fp and the membrane anchor, indicating that the overall structural stability of the complex is conferred by the Ip protein.

The contact surfaces between the four subunits are dominated by hydrophobic interactions. Compared with the solvent-accessible surface in general, the contact surface possesses significantly lower thermal factors (Figure 3C), which is in good agreement with the strong binding of those subunits. In addition, one novel helix-loop motif (C6–C34, helix 1L) at the N terminus of CybL protrudes into the matrix side, where it interacts with Ip via a surface contact area of 900 Å^2 and contributes about 40% of the contact area between Ip and the transmembrane anchor. The only linkage between helix 1L and the main body of the hydrophobic membrane anchor is mediated by a flexible loop (C22–C35). These unique properties of helix 1L suggest that it is important for the stability of Complex II and may play a crucial role in recognition between Ip and the transmembrane anchor when this complex is being assembled.

Prosthetic Groups

The five prosthetic groups (FAD, [2Fe-2S], [4Fe-4S], [3Fe-4S], and heme group) required for electron transfer from succinate to ubiquinone were unambiguously assigned into the electron density map (Figure 4A).

FAD is located at the interface of the β barrel subdomain and the embedded subdomain of Fp and is directed into the β barrel (Figure 3B). A covalent bond was found between C8M of FAD and NE2 of His-A57. There were hydrogen bonds between FAD and Fp main-chain atoms of Lys-A50, Gly-A65, Ala-A179, Asn-A413, Ser-A414, and Leu-A415 and side chain atoms of Thr-A49, Ser-A56, Asp-A233, Ser-A414, and Glu-A398.

Ip binds the three iron-sulfur clusters (Figures 3B and 4A). First, in the B64–B73 loop region, [2Fe-2S] is tightly ligated by four conserved cysteines: Cys-B65, Cys-B70, Cys-B73, and Cys-B85. Second, [4Fe-4S] binds to the loop region (B158–B164 and B224–B229) though

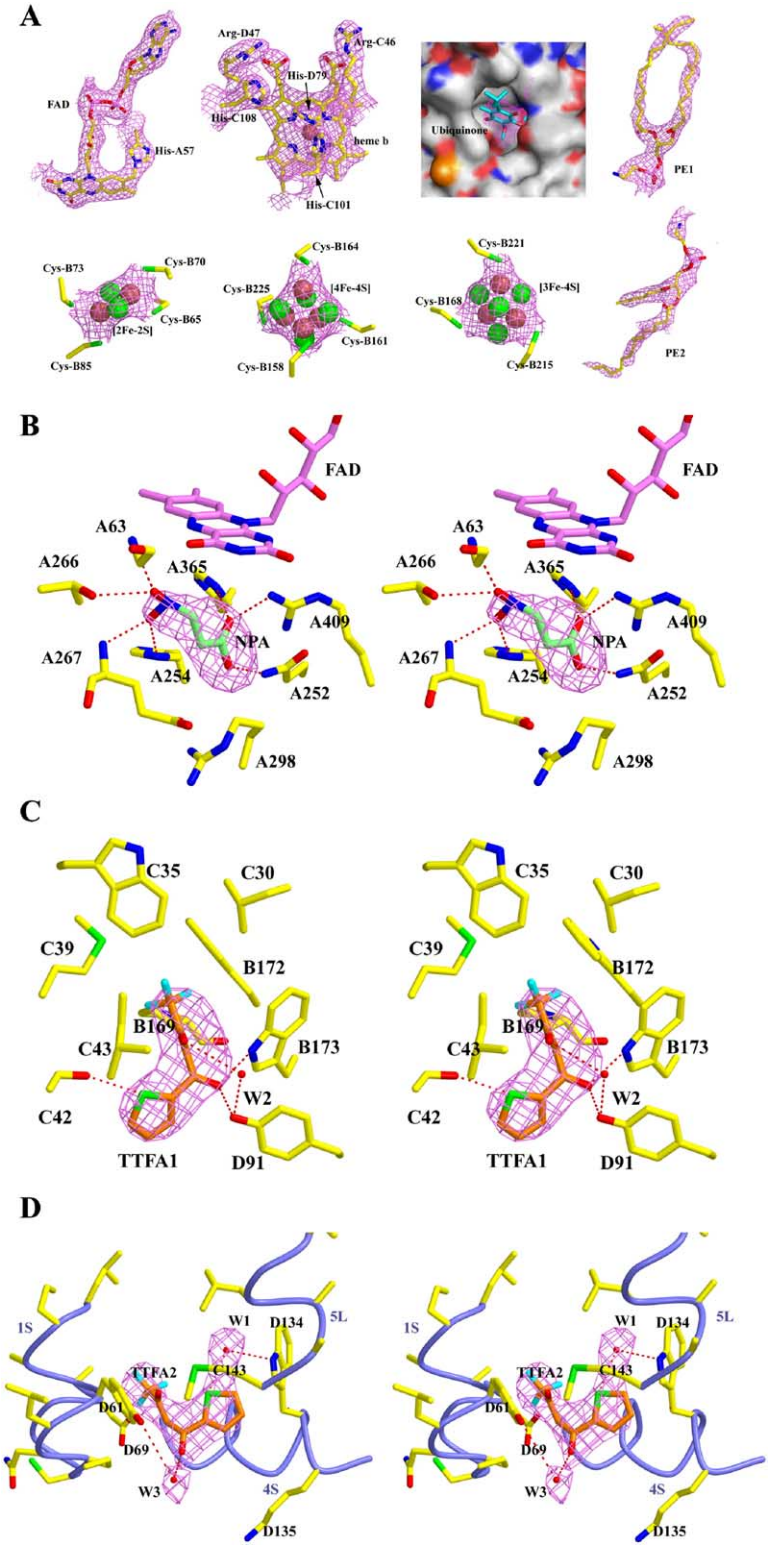

Figure 4. The Prosthetic Groups, Phospholipids, Inhibitors, and Ubiquinone

(A) The prosthetic groups FAD, [2Fe-2S], [4Fe-4S], [3Fe-4S], and heme b are shown together with their coordinating ligands. All prosthetic groups are covered by a $2F_o - F_c$ map, with FAD and heme b contoured at 1.2 σ and the iron-sulfur clusters contoured at 3 σ. Ubiquinone is shown in the Qp binding site and covered by a composite omit map contoured at 0.8 σ. Two phospholipids, PE1 and PE2, are shown and covered by an omit map contoured at 1.0 σ.

(B) Stereoview of the succinate binding pocket with the inhibitor 3-nitropropionic acid (NPA) covered by an omit map contoured at 3.0 σ.

(C) Stereoview of the ubiquinone binding pocket (Qp) occupied by the inhibitor 2-thenoyltrifluoroacetone (TTFA1). TTFA1 is covered by an omit map contoured at 3.0 σ.

(D) Stereoview of the ubiquinone binding pocket (Qd) occupied by the inhibitor 2-thenoyltrifluoroacetone (TTFA2). TTFA2 is covered by an omit map contoured at 2.6 σ. Hydrogen bonds are shown in red dashed lines, and residues around these inhibitors are labeled.

four cysteine ligands: Cys-B158, Cys-B161, Cys-B164, and Cys-B225. Third, around [3Fe-4S] are two loops, B215–B221 and B167–B171, where the side-chain thiolates of Cys-B221, Cys-B168, and Cys-B215 take the role of ligands to the iron centers.

As shown in Figure 3B, the heme group is embedded into the transmembrane region among the four bound helices (helices 2L, 4L, 1S, and 2S). The heme iron is coordinated by the imidazole of two histidines, His-C101 and His-D79, with the same Fe-N distance of

2.2 Å. The heme propionate groups interact with three charged residues, Arg-D47, His-C108, and Arg-C46 (Figure 4A). The hydrophobic interaction between the porphyrin group and four helices further stabilizes the bound heme.

Phospholipids

In the native structure, clear electron density for two long acyl chains was located among helix 2L, helix 4L, and helix 1S below the heme group, and this was assigned as a phospholipid. The mitochondrial inner membrane is mostly composed of cardiolipin (CL), phosphatidylethanolamine (PE) and phosphatidylcholine (PC). Based on the shape of the electron density, we assigned the lipid as PE (Figures 3A and 4A). The binding of this PE lipid, termed PE1, shows a tight and hydrophobic mode with two long acyl tails, and no specificity could be found for its head binding. A second phospholipid, also assigned as phosphatidylethanolamine (PE2), was located near helix 3S (Figure 4A). This second phospholipid becomes a mediator for transmembrane interactions when those complexes pack together in the crystal. It is interesting to note that no phospholipid molecules could be found at equivalent positions in the complex structure cocrystallized with inhibitors NPA and TTFA.

Inhibitors

3-nitropropionate (NPA) is a succinate analog and a strong inhibitor for the succinate-oxidation enzymatic activity of Complex II. 2-thenoyltrifluoroacetone (TTFA) is a classical inhibitor for the ubiquinone reduction of Complex II by occupying its ubiquinone binding sites. The Complex II and these two inhibitors were cocrystallized in the same orthorhombic crystal form (space group $P2_12_12_1$) and unit cell as the native structure. The final inhibitor binding complex model was refined to 3.5 Å resolution. One NPA molecule (Figure 4B) was found near the FMN group of FAD, and two TTFA molecules (Figures 4C and 4D) were found in the proximity of [3Fe-4S] and at the distal side of the transmembrane anchor.

Electron density in the omit map at the succinate binding site was assigned as an NPA molecule (Figure 4B). The nitryl group of NPA interacts with the side chains of Thr-A266 and His-A254, the main chains of Glu-A267 and Gly-A63, and the FMN group of FAD. The amide group of Gln-A252 anchors one side of the carboxyl group of NPA, while the guanidinium group of Arg-A409 and the imidazole group of His-A365 anchor the other side. It is notable that this substrate binding site near FAD is empty but for a few bound water molecules in the native Complex II structure.

One TTFA molecule (TTFA1) could be clearly assigned according to the omit map (Figure 4C). TTFA1 binds to the pocket formed by helix 2L (C38–C52), helix 2S (D77–D91), and the [3Fe-4S] ligating region (B214–B219 and B166–B175), which will be discussed below. The oxygen atom from the thenoyl group forms two hydrogen bonds with the side chains of Trp-B173 and Tyr-D91, and another oxygen atom from the trifluoroacetone group interacts with the side chain of Tyr-D91 via one water molecule (W2) as a mediator. The sulfur atom from the thenoyl group interacts with the hydroxyl group of Ser-C42. The hydrophobic environment formed by residues Trp-C35, Met-C39, Ile-C43, Ile-C30, Pro-B169, and Trp-B172 is favorable for TTFA binding, especially for the fluoroform and thiophene groups.

Density in the omit map near the C terminii of CybL and CybS could be assigned as a second TTFA molecule (TTFA2) (Figure 4D). Two water molecules surround the inhibitor and are thought to be mediators for interactions between TTFA2 and Complex II. The oxygen atom of the thenoyl group interacts with the side-chain atom of Tyr-D61 via water W3. The interaction between the sulfur atom of the thenoyl group and the side chain of Trp-D134 is mediated by water W1. TTFA2 occupies the position quasiequivalent to the head group of the PE1 phospholipid found in the native structure. Assuming the missing phospholipid was not due to the sample preparation process, this inhibitor-phospholipid exchange should have biological significance.

The fact that TTFA1 has stronger electron density than TTFA2 suggests that the binding affinity for TTFA1 is higher than for TTFA2, which is also confirmed by the different binding modes for those two molecules: TTFA1 interacts with Complex II more directly via more hydrogen bonds and more hydrophobic contacts than TTFA2, which interacts mainly through two water molecules.

Ubiquinone and Its Binding Sites

Biochemical studies have indicated that there are at least two ubiquinone binding sites in eukaryotic mitochondrial SQR. One site (Qp) is on the matrix side, and the second (Qd) is near the intermembrane-space side (Hagerhall, 1997). The Qp and Qd sites were investigated by mutagenesis studies in yeast mitochondrial SQR, and several residues were identified that could function as ubiquinone binding ligands (Oyedotun and Lemire, 1999; Oyedotun and Lemire, 2001). Kinetic analysis with specific inhibitors of mammalian mitochondrial Complex II also gave clues for the existence of two ubiquinone binding sites (Yankovskaya et al., 1996). Residues related with ubiquinone binding were probed for CybL (QPs1) and CybS (QPs3) of bovine Complex II using a photoaffinity-labeling method (Lee et al., 1995; Shenoy et al., 1999; Shenoy et al., 1997), and their roles would be interpreted after determination of the Complex II structure.

Comparison of the Complex II structure with the superimposed *E. coli* SQR structure (PDB ID code 1NEK) (Yankovskaya et al., 2003) around the [3Fe-4S] cluster readily revealed the location of the Qp site (Figure 5A), which is formed by helix 2L (C38–C52), helix 2S (D77–D91), and the [3Fe-4S] ligating region (B214–B219 and B166–B175). In addition, both the $2F_o - F_c$ and the composite omit map showed electron density within this site that was fitted with the head group of a bound ubiquinone molecule (Figure 4A). No density was observed for the long isoprenoid tail, although a long sunken hydrophobic channel below this binding cavity and formed by helix 2L and helix 3S could accommodate its shape and size (Figure 5B). The environment around this region is similar in both eukaryotic and prokaryotic SQR structures, and the specific residues Trp-

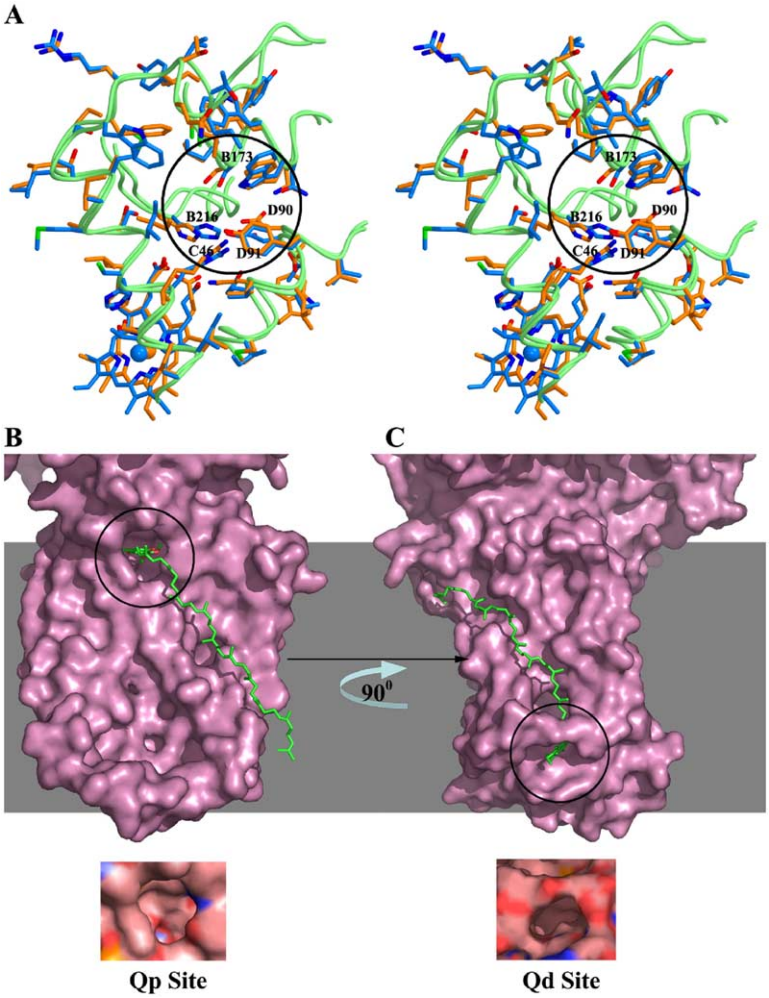

Figure 5. Ubiquinone Binding Sites

(A) Stereoview showing the superposition of Qp pocket regions (circled) based on the overall C_α atoms from mitochondrial SQR and *E. coli* SQR. Residues in the Qp site are shown in blue for mitochondrial SQR and gold for *E. coli* SQR. Both C_α traces are shown in green. Important residues are labeled for mitochondrial SQR.

(B and C) The conserved Qp site (B) and the Qd site (C). SQR is shown in surface representation (drawn using PyMol 0.98). Ubiquinone-10, schematically, is shown (in green) placed into the respective binding sites (circled). Surface-cavity representations of the Qp and Qd sites are shown underneath, with nitrogen atoms colored blue and oxygen atoms colored red.

B173, His-B216, Ser-C42, Arg-C46, Tyr-D91, and Asp-D90 are conserved for substrate binding and catalytic activity (Figure 5A), as previously proposed. Hydrogen bonds between Trp-B173, Tyr-D91, and the oxygen O1 of ubiquinone contribute to the binding specificity, and Asp-D90 and Arg-C46 are suggested to play functional roles in the protonation of ubiquinone upon reduction (Yankovskaya et al., 2003). In the inhibitor bound complex structure, TTFA1 binds to this Qp pocket as described above. Trp-B173, Try-D91, and Ser-C42 are responsible for its binding, and the clear and strong electron density suggests its high binding affinity. This tightly bound TTFA1 molecule further confirms the existence of the Qp site and its location. The conservation of the Qp binding pocket from *E. coli* to mammalian SQR implies a similar mechanism of electron transfer from succinate to ubiquinone at the Qp site.

Near the intermembrane side, with the aid of the bound TTFA2 inhibitor, we identified a second ubiquinone binding pocket (Figure 4D) formed by the loop between helix 1S and helix 2S, helix 4S, and the C terminus of CybL (helix 5L) and lined by the residues Trp-D134, Lys-D135, and Tyr-D61. As observed above for the proposed Qp binding pocket, there is also a long sunken hydrophobic channel formed by helices 1S, 4L, and 5L, which could accommodate the long isoprenoid tail of ubiquinone (Figure 5C). In the mitochondrial system, one distal ubiquinone binding site (Qd) has been proposed to exist on the opposite side of the membrane from the Qp site (Hagerhall, 1997). From the view of this structure and the bound TTFA2 inhibitor, we are encouraged to propose this pocket as the candidate for the Qd site. The residues Trp-D134 and Tyr-D61 at the Qd site would confer its specificity for ubiquinone binding, and residues Lys-D135 and Asp-D69 near this pocket could take the functions of ubiquinone protonation. Those residues are highly conserved among mammalian mitochondrial Complex II (Figure 2B). As mentioned above, the binding affinity for TTFA at the Qp site is expected to be higher than at the Qd site. This is in line with experiments by Yankovskaya and coworkers, who found one strong and one weak inhibitor binding site in the reaction for ubiquinone reduction (Yankovskaya et al., 1996).

The ubiquinone binding-related sequence on CybL (QPs1) of bovine Complex II is GLTISQL and is located at residues 113–119 (Lee et al., 1995). The equivalent sequence in our structure is from C116 to C122, located between helices 4L and 5L, and is not exactly the same but is close to the observed Qp pocket. The related

sequence on CybS (QPs3) of bovine Complex II is LNPCSAMDY and corresponds to residues 29–37 (Shenoy et al., 1997; Shenoy et al., 1999). The equivalent sequence in the structure is from D62 to D70, in the loop region between helix 1S and helix 2S, which is near the Qd site. These minor disaccords may result from the inaccuracy of the photoaffinity-labeling method and the inexact conformation of recombinant CybL (QPs1) and CybS (QPs3).

In addition, the EPR (electron paramagnetic resonance) signal (g = 2.0) indicated a radical semiubiquinone pair (the distance between each other is approximately 8.0 Å, assuming dipole-dipole interaction) in close proximity to the [3Fe-4S] cluster (Ingledew et al., 1976; Ohnishi and Trumpower, 1980; Ruzicka et al., 1975; Salerno et al., 1977), suggesting that there are probably two ubiquinone sites at the proximal side. However, checking the putative cavities at the matrix side near the Qp site, we could not find any additional electron density that could be assigned as ubiquinone. Furthermore, in the complex structure bound with inhibitors, no other electron density could be found for a second TTFA molecule near the Qp site. As described in the literature, the EPR signal derived by semiubiquinones is sensitive to TTFA. Combining this information with the TTFA bound complex structure leads us to conclude that the Qp site could also bind and stabilize a semiubiquinone. A second putative ubiquinone binding site near Qp was not observed and may reflect its lower affinity for TTFA.

Comparison with *E. coli* SQR

Comparison between mitochondrial SQR and *E. coli* SQR highlights those structural differences that result in significant functional changes as well as confirming conserved structural components. A sequence alignment (see Supplemental Data) calculated using ClustalW 1.7 (Thompson et al., 1994) for mitochondrial and *E. coli* SQR indicates that the homologies for Fp and Ip are 51% and 50%, respectively. The similarity between Fp and Ip in the two SQR structures is confirmed by superposition (Figures 6A and 6B). The root-mean-square-deviation value is 1.0 Å for 541 matched out of 613 C_α atoms of Fp protein (with a 2.0 Å cutoff), and 0.8 Å for 214 matched out of 249 C_α atoms of Ip protein. There are two obvious insertions in the porcine Fp structure, from A561 to A578 (Figure 6A, region 1) and from A135 to A143 (Figure 6A, region 3), and one deletion at A122–A123 (Figure 6A, region 4) (there is one loop from A110 to A117 in the *E. coli* structure).

In contrast to the strong homology for Fp and Ip between mitochondrial and bacterial SQRs, the homologies for CybL and CybS are as low as 19% and 18%, respectively (Figures 2A and 2B). There is a large divergence in the membrane-anchor proteins of mitochondrial and *E. coli* SQR (Figure 6C), as evidenced by the root-mean-square deviations of 1.3 Å for 76 matched out of 138 total C_α atoms of CybL and 1.7 Å for 79 matched out of 102 total C_α atoms of CybS. The topology divergence of secondary-structure elements is even larger: 10.2 Å for CybL and 5.6 Å for CybS, as calculated by Top3d (Lu, 2000). CybL of mitochondrial SQR possesses one N-terminal helix that interacts favorably with Ip, while *E. coli* SQR has only one irregular β strand. The angle (~60°) between helix 2L and helix 4L in mitochondrial SQR is larger than that (~40°) between helix e1L and helix e3L of the *E. coli* enzyme, resulting in the obvious sunken hydrophobic region described above (Figure 3A). CybS of mitochondrial SQR shows transmembrane folding markedly different from its counterpart in *E. coli* SQR. Helix 4S is located at the bottom of the structure and is antiparallel to helix 3L, while helix 3S lies around the bound transmembrane core. In *E. coli* SQR, however, helix e4S is located around the transmembrane core with helix e2S situated below. The differences in the membrane anchors result in a thinner transmembrane domain for mitochondrial SQR (data not shown) and allow for additional semipolar cavities that may serve as ubiquinone binding pockets (Qd), as discussed above (Figure 5C).

Mitochondrial and *E. coli* SQR share near-equivalent positions for FAD, the three iron-sulfur clusters in the hydrophilic head, and one heme group in the hydrophobic tail. However, several residue changes around the three iron-sulfur clusters result in altered environments for these prosthetic groups that should account for the different redox potentials of the clusters (Figure 3A).

In detail (Figure 6D), residue Cys-B73, which ligates to [2Fe-2S] and is conserved among mitochondrial SQR, is substituted by Asp-B63 at the equivalent position in *E. coli* SQR. Around the [4Fe-4S] cluster, the changes are from Leu-B176 and Ala-B177 in *E. coli* SQR to Met-B185 and Gln-B186 (both of which interact with the cluster through one water molecule) in mitochondrial SQR, which would account for the redox potentials of –175 mV in *E. coli* SQR and –260 mV in mitochondrial SQR (Hagerhall, 1997). Furthermore, Phe-B169 in *E. coli* SQR is substituted by Tyr-B178 in mitochondrial SQR. Although the phenol side chain of Tyr-B178 interacts with the [3Fe-4S] cluster, there is only a modest shift in the redox potential (from +65 mV to +60 mV) (Hagerhall, 1997).

A preponderance of polar residues located around the heme molecule in mitochondrial SQR instead of hydrophobic residues in *E. coli* SQR could account for the different redox potentials of the mitochondrial-SQR heme b molecule (–185 mV) (Yu et al., 1987) and its counterpart in *E. coli* (+36 mV) (Yankovskaya et al., 2003). The heme b molecule is locked into position by two histidines, His-C101 and His-D79, and supported by two arginine residues, Arg-C46 and Arg-D47. The Fe-N (imidazole) distances (2.2 Å) in mitochondrial SQR are not abnormally short, and there are no residues close to the imidazole ligands that can form H bonds to the nitrogens to render the imidazole a stronger donor by imparting imidazolate character to the ring. Residues surrounding the heme in mitochondrial SQR include Glu-D46, Ser-D50, Thr-C102, Asn-C104, Thr-C48, and Ser-C53, while there are Val-D19, Ala-D23, Val-C85, Val-C87, Ser-C33, and Phe-C38 at equivalent positions in the *E. coli* structure (Figure 6E). The more polar environment in mitochondrial SQR around the heme could be a significant factor in lowering the heme redox potential. It should be noted that although midpoint redox potential data were measured from bovine SQR (Hagerhall, 1997; Yu et al., 1987), they are believed to be exactly the same for porcine SQR.

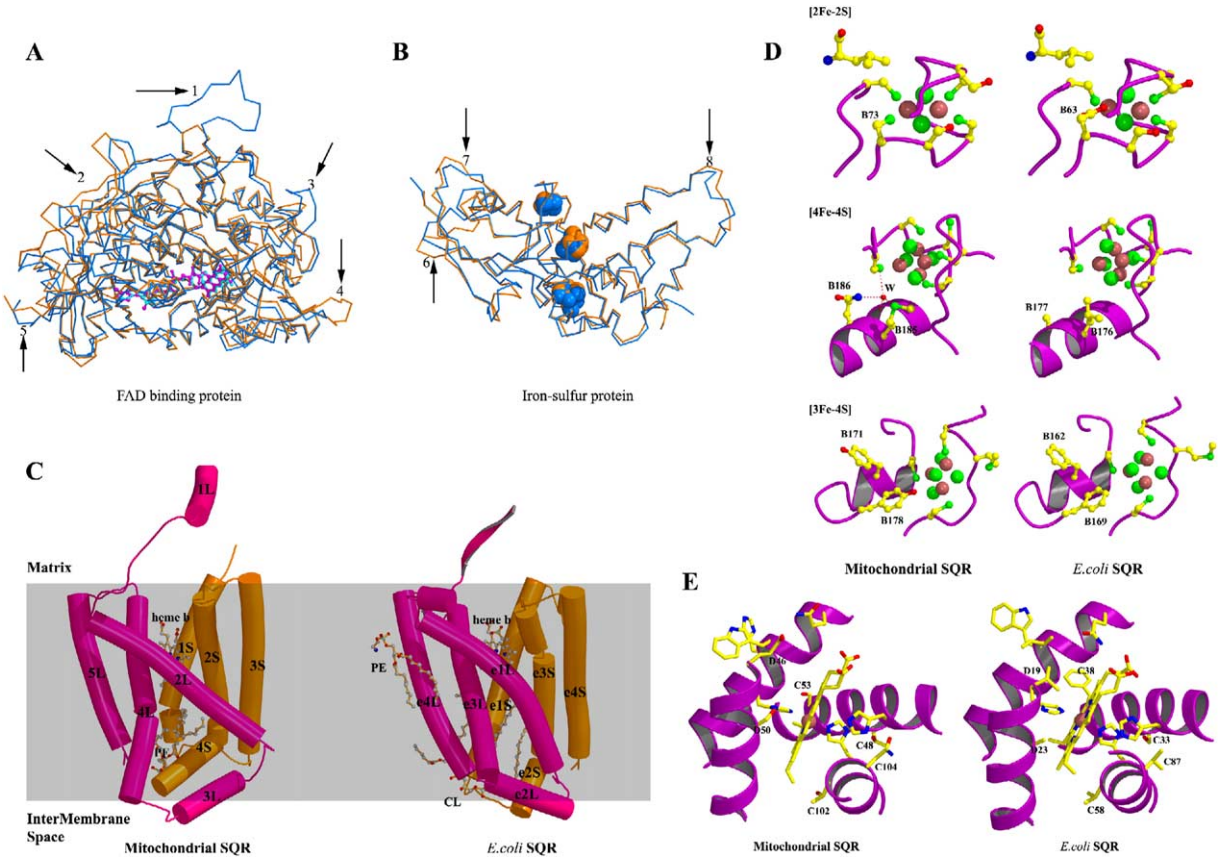

Figure 6. Comparison between Mitochondrial and *E. coli* SQR Structures

(A and B) Comparison between mitochondrial and *E. coli* SQR structures for (A) Fp and (B) Ip. The mitochondrial SQR structure is shown in blue and the *E. coli* SQR in gold. Large deviations are marked by arrows, numerically labeled, and discussed in the main text.

(C) Comparison between the transmembrane helices of mitochondrial (left) and *E. coli* (right) SQR structures. CybL is shown in pink and CybS in gold. Helices 1L–5L (e1L–e4L) in CybL and helices 1S–4S (e1S–e4S) in CybS are labeled.

(D) Differences in environments of the iron-sulfur clusters between mitochondrial (left) and *E. coli* (right) SQR structures. The [2Fe-2S], [4Fe-4S], and [3Fe-4S] clusters are shown, with ligating residues shown in ball-and-stick representation.

(E) Differences in environments of the heme b group between mitochondrial (left) and *E. coli* (right) SQR structures. The heme b group and ligating residues are shown in stick models.

Residues Related with Mitochondrial Diseases

A number of diseases, such as familial or nonfamilial head-and-neck paraganglioma, familial or nonfamilial pheochromocytoma, midgut carcinoid tumors, Merkel cell carcinoma, and Leigh syndrome, are known to be caused by defects in the mitochondrial respiratory system and are mainly associated with mutation or truncation of Complex II (Ackrell, 2002; Astuti et al., 2001a; Astuti et al., 2001b; Baysal et al., 2000; Bourgeron et al., 1995; Douwes Dekker et al., 2003; Ishii et al., 1998; Niemann and Muller, 2000; Rustin and Rotig, 2002). In certain cases, a nucleotide change leads to a premature stop codon, resulting in a C-terminal truncation in the corresponding Complex II protein. A nucleotide change also leads to an altered start codon, resulting in proteins without a mitochondria-location signal peptide. More importantly, previous work showed that point mutation, insertion, or truncation of mitochondrial SQR causes electron leakage from the prosthetic groups in the electron transfer chain, producing reactive oxygen species (ROS) and leading to tumor formation. Under normal circumstances, electrons could escape from the FAD group and the Qp site (Guo and Lemire, 2003; Messner and Imlay, 2002). However, mutated residues around the iron-sulfur clusters and heme b molecule may also produce heavy electron leakage, which is even more dangerous for mitochondria.

SQRs from mammalian mitochondrial membranes share very high sequence similarity, and, in particular, the respective sequence homologies of subunits A, B, C, and D between human and porcine are 95%, 98%, 92%, and 90%, respectively (see Figure 2 and Supplemental Data). Because of the very high sequence and structural homology between porcine and human SQRs, we attempt to provide structural explanations for the relationship between the malfunction of mitochondrial SQR and various mutations associated with the diseases (Table 2). These rational explanations may provide clearer guidance for clinic diagnostics, gene therapy, and drug design for the treatment of these diseases. For example, mutation of Cys to Tyr at position B73 expands the [2Fe-2S] ligating pocket and de-

Table 2. Structure-Based Explanations for Mitochondrial Diseases Related with Defects in Complex II

Subunit	Point Mutation	Disease and Phenotype	Explanation Based on Structure
A	Arg-A409 → Cys (Birch-Machin et al., 2000)	Optic atrophy, ataxia, myopathy	Altering succinate binding specificity
	Ala-A482 → Val (Parfait et al., 2000)	Leigh syndrome	?
	Arg-A512 → Trp (Bourgeron et al., 1995)		Unstable Fp helix domain
	Gly-A513 → Glu (Van Coster et al., 2003)		Unstable Fp helix domain
B	Cys-B73 → Tyr (Neumann et al., 2002)	Phaeochromocytoma	Destroys the ligation of [2Fe-2S]
	Pro-B103 → Arg (Baysal et al., 2002)	Head-and-neck paraganglioma	No room for this large residue
	Cys-B164 → Arg (Neumann et al., 2002)	Phaeochromocytoma	Destroys the ligation of [4Fe-4S]
	Cys-B168 → Tyr (Neumann et al., 2002)		Destroys the ligation of [3Fe-4S]
	Pro-B169 → Arg (Astuti et al., 2001b)		Changes the [3Fe-4S] ligation conformation and destroys the ubiquinone binding site (Qp)
	Arg-B214 → His (Neumann et al., 2002)		Might change the pK value of Asp-D90, then influence the protonation of ubiquinone (Qp)
	Cys-B221 → X (Neumann et al., 2002)		Destroys the ligation of [3Fe-4S]
C	Leu-C132 → Pro (Bauters et al., 2003)	Paraganglioma	Destroys the stability of helix 5L, then might destroy the ubiquinone tail binding (Qd)
D	Arg-D47 → Gly (Taschner et al., 2001)	Head-and-neck paraganglioma	Destroys the interaction with the heme b carboxylate group
	Pro-D58 → Leu (Baysal et al., 2000)	Head-and-neck paraganglioma	Changes the folding of helix 1S, then destroys the ubiquinone binding site (Qd)
	Asp- D69 → Tyr (Baysal et al., 2000)	Head-and-neck paraganglioma/ phaeochromocytoma	Might lose the catalytic activity for ubiquinone reduction (Qd)
	Leu-D72 → Pro (Taschner et al., 2001)	Head-and-neck paraganglioma	Changes the folding of helix 2S, then the position of one heme b ligand, His-D79
	His-D79 → Leu (Baysal et al., 2000)		Destroys the ligation of heme b
	Tyr-D91 → Cys (Milunsky et al., 2001)		Destroys the binding of ubiquinone (Qp)
	Gln-D98 → X (Neumann et al., 2002)	Phaeochromocytoma	Helices 3S and 4S missing
	Leu-D116 → Pro (Taschner et al., 2001)	Head-and-neck paraganglioma	Changes the folding of helix 3S, then destroys the Qd site

stroys its ligation. In this instance, electrons can no longer be transferred from FAD to [4Fe-4S] but instead leak into the matrix, thus producing ROS and resulting in phaeochromocytoma symptoms. In another instance, mutation of His to Leu at D79 eliminates the interaction between this histidine and the heme iron, thus abolishing ubiquinone reduction at the Qp site. Consequently, electron transfer is truncated at the iron-sulfur clusters, resulting in leakage into the membrane and production of ROS, which manifests itself as head-and-neck paraganglioma symptoms.

Implications from the Mitochondrial Complex II Structure

Two changed residues around the [4Fe-4S] cluster result in a large decrease in redox potential, which could be essential for the electron transfer rate. The three iron-sulfur clusters of SQR provide a direct pathway for electron transfer without any preferred direction. The electron transfer direction only depends on the redox potential of the terminal acceptor compared with the start donor. In particular, the lower redox potential of [4Fe-4S] increases the energy barrier for electron transfer and, more importantly, might avoid electron flow in the reverse direction in mitochondrial SQR.

The five prosthetic groups, together with ubiquinone at the Qp site, are arranged in a linear path with favorable distances for electron transfer (Figure 3A). The edge-to-edge distances between FAD and the 2Fe-2S cluster, and between the different iron-sulfur clusters, are each less than 14 Å, which is favorable for direct electron transfer (Page et al., 1999). Classical dogma asserts that electrons are transferred from succinate to ubiquinone though FAD, [2Fe-2S], [4Fe-4S], [3Fe-4S], and heme b sequentially. However, examination of the distances between these redox centers in mitochondrial SQR suggests that it would not be favorable for heme b to mediate electron transfer from [3Fe-4S] to ubiquinone. The edge-to-edge distance is about 7.1 Å between the bound ubiquinone at the Qp site and [3Fe-4S], about 13.3 Å between [3Fe-4S] and heme b, and about 11.4 Å between heme b and ubiquinone. These distances suggest that it is not necessary for electrons to transfer to ubiquinone through a mediator heme b. Furthermore, the redox potential of heme b (–185 mV) is much lower than that of [3Fe-4S] (+60 mV), which also suggests that ubiquinone reduction (+113 mV) is more favorable than heme b reduction. However, once heme b is reduced, it can reduce ubiquinone because the reaction is favorable and the distance is suitable for electron transfer.

The mitochondrial Complex II structure bound with

inhibitors confirms the existence of a Qd site near the intermembrane side, revealing a new electron transfer pathway. The distance between the Qd site and the edge of heme b is about 15 Å, and ubiquinone bound at the Qd site with proper conformational changes is thought to be able to accept an electron from heme b. Electrons from succinate oxidation could then transfer through three iron-sulfur clusters and the heme b molecule to ubiquinone at the Qd site. The two ubiquinone binding sites, one at the matrix side (Qp) and the other at the intermembrane side (Qd), would result in a branching of electron transfer. Ubiquinone at the Qp site would obtain electrons first due to its favorable position, then electrons would be transferred to ubiquinone in the Qd site after reduction at the Qp site becomes saturated.

The presence of two ubiquinone binding sites would favor the transfer of two electrons from reduced $FADH_2$ to ubiquinones with high efficiency. As a result, semiubiquinones should be stabilized for a longer time to accept further electrons, which is in agreement with the observed semiubiquinone signals in EPR studies (Ingledew et al., 1976; Miki et al., 1992; Ohnishi and Trumpower, 1980; Ruzicka et al., 1975; Salerno et al., 1977; Xu et al., 1987). Tyr-D91 at the Qp site, considered as an important residue for the stability of the semiubiquinone (Yankovskaya et al., 2003), is conserved in all SQR but is not found in QFR of *E. coli*. Tyr-D61 at the Qd site is believed to play the same role in stabilizing semiubiquinone and is also conserved in mammalian mitochondrial SQR. The mechanism of ubiquinone binding and stabilization remains to be investigated by further determination of mitochondrial SQR structures in complex with selected ubiquinone analogs.

From the mitochondrial SQR structure, only one clear ubiquinone is observed at the Qp site. One explanation is the different ubiquinone binding affinities for different sites. This difference provides new insight into the role of Complex II in the mitochondrial respiratory chain. It is only the mitochondrial Complex II that couples the Krebs cycle with the electron transfer chain, and it should also provide a feedback mechanism. The main electron transfer chain is $NADH_2$ → Complex I → UQ → Complex III (bc_1) → Cyt c → Complex IV → O_2. $NADH_2$ is produced in the Krebs cycle. The key step of the Krebs cycle, in which succinate is oxidized to fumarate, is driven by Complex II (Figure 1). Although the potential derived from the oxidation of succinate to fumarate is not large (about +30 mV), this reaction is mostly driven by the reduction of ubiquinone to ubiquinol with a redox potential of +113 mV. The concentrations of ubiquinone/ubiquinol, as well as their binding affinities, are closely correlated with the rate of the Krebs cycle through Complex II according to the Nernst equation. As a consequence, the rate of fumarate production would be transformed by the modulated rate of the Krebs cycle, thus maintaining the balance between energy storage and conversion.

Conclusions

The first crystal structure of porcine mitochondrial respiratory Complex II (succinate:ubiquinone oxidoreductase) has been determined at 2.4 Å resolution as well as its complex structure with two inhibitors, 3-nitropropionate (NPA) and 2-thenoyltrifluoroacetone (TTFA), at 3.5 Å resolution, providing a bona fide model for understanding the mitochondrial respiratory system and the ubiquinone-reduction mechanism of Complex II at an atomic level. Comparing the overall structure with *E. coli* SQR, we find striking differences in environments surrounding the prosthetic groups, resulting in significant shifts in the midpoint redox potential. Furthermore, substantial differences in the transmembrane regions of mitochondrial SQR and *E. coli* SQR clearly demonstrate the limitations of *E. coli* SQR as a model for investigating ubiquinone binding sites in mitochondrial SQR. On the basis of the mitochondrial SQR structure presented here, two proposed ubiquinone binding sites have been discussed. One proximal (Qp) ubiquinone binding pocket is found to be conserved from prokaryotes to eukaryotes. Near the C terminii of CybL and CybS, another pocket is thought to be the distal (Qd) ubiquinone binding site. The crystal structure of the mitochondrial Complex II provides a framework for investigating these ubiquinone binding pockets. Their existence is further supported by the clear binding of two specific TTFA inhibitors. Several important residues, belonging to the four subunits of Complex II, are highlighted for their implication in mitochondrial diseases.

Experimental Procedures

Preparation of Complex II from Porcine Heart

The preparation of Complex II from porcine heart is described in the Supplemental Data.

Crystallization and Data Collection

The prepared SQR (~50 mg/ml) with 25 mM HEPES (pH 7.2) buffer, 400 mM sucrose, 200 mM NaCl, and 1 mM EDTA was diluted with precooled 25 mM HEPES (pH 7.2) to a final concentration of about 25 mg/ml. The detergent *n*-nonyl-β-D-maltoside was added to a final concentration of 0.5% (w/v). After solubilization by detergent, the SQR preparation was centrifuged at 15,000 × g for one hour. The pellet was discarded and the supernatant collected for crystallization.

SQR was crystallized as a hanging drop consisting of 2 μl of 25 mg/ml protein solution and 2 μl of crystallization solution comprised of 25 mM HEPES (pH 7.2), 5% (w/v) PEG 4000, 3% (w/v) 1,6-hexanediol, 100 mM NaCl, and 10 mM $CaCl_2$ against 200 μl reservoir solution containing 12% (w/v) PEG 4000, 3% (w/v) 1,6-hexanediol, 200 mM sucrose, and 200 mM NaCl. In addition, if 0.4 μl of *n*-decyl-β-D-maltoside (1.7 mM) was added to the crystallization mixture as an additive, better crystals were obtained. Crystals appeared after 2 days at room temperature and gained their shape and high diffraction quality after a further 2–3 days.

To obtain SQR in complex with bound inhibitors, the succinate analog 3-nitropropionate (NPA) and the ubiquinone-reduction inhibitor 2-thenoyltrifluoroacetone (TTFA) were added together into the protein sample at a final concentration each of 2 mM and incubated for 1 hr. The same crystallization condition was applied to this sample. Two days later, complex crystals formed with good shape but small size compared with native crystals.

Most native crystals diffracted to 4.0 Å in-house and a few diffracted to 3.5–3.0 Å resolution. Diffraction by each crystal showed obvious anisotropic distribution beyond 4.0 Å. One set of SAD data was collected to 3.0 Å resolution at the iron-K edge (λ = 1.74101 Å) and another high-resolution native data set was collected to 2.4 Å resolution (λ = 1.0322 Å). For the SQR inhibitor complex, one data set was collected from a single crystal to 3.5 Å resolution (λ = 0.9793 Å). All data were collected from beamline BL19-ID of the Advanced Photon Source (APS), Argonne National Lab. Data were

processed, integrated, merged, and scaled using HKL2000 (Otwinowski and Minor, 1997). The unit-cell parameters of porcine SQR crystal (native or complex) are a = 70.2 Å, b = 83.5 Å, c = 293.9 Å, $\alpha = \beta = \gamma = 90°$ with space group $P2_12_12_1$.

Structure Determination

Mitochondrial SQR contains ten intrinsic irons, which were used for initial determination of experimental phases. One single-wavelength anomalous diffraction (SAD) data set was collected up to 3.0 Å resolution at the iron-K absorption edge. Four heavy-atom positions were calculated using SOLVE (Terwilliger and Berendzen, 1999) based on Patterson research and represent the center positions of three iron-sulfur clusters ([2Fe-2S], [4Fe-4S], and [3Fe-4S]) and one heme molecule. Assuming one complex per asymmetric unit, the initial anomalous map was used to locate ten irons, from which initial phases were calculated up to 3.5 Å resolution. Density modification was performed and the phases were extended to 3.0 Å using CNS (Brunger et al., 1998). The initial map was generally of poor quality, but the transmembrane region with six helices could be clearly recognized. Molecular replacement (using the *E. coli* SQR crystal structure, PDB ID code 1NEK, as the search template) and phase combination further improved the phases. The initial model of two hydrophilic subunits of mitochondrial SQR was generated by Modeller7 (Marti-Renom et al., 2000) according to the structure of *E. coli* SQR and used to calculate a rotation function. After translation in real space using the previous phases, a significant map-fitted solution was found with CNS (Brunger et al., 1998), with correlation coefficient 0.25 and reasonable packing. After rigid-body refinement, phases from the translated model were combined with the experimental phases, resulting in a significantly improved electron density map. With this map, the initial model of mitochondrial SQR was built using the program O (Jones et al., 1991), with C_α atoms only for two hydrophobic proteins.

After a few cycles of model building, refinement, and phase combination, another data set collected and processed to 2.4 Å resolution was used for further model building, residue discrimination, and refinement. Initial phases for this new data set were calculated using the crude initial model and significantly improved after density modification, such that the electron density map was clear enough to build the whole model in O (Jones et al., 1991). After several cycles of refinement, one FAD molecule and two phospholipid molecules were added into the model. The $F_o - F_c$ electron density map and omit density map were used to assign the head of the ubiquinone molecule according to the conserved binding site. The model was refined to a final R_{work} = 21.3% and R_{free} = 25.9% and confirmed to have good stereochemistry from a Ramachandran plot calculated by PROCHECK (Laskowski et al., 1993).

The refined model including five prosthetic groups was used to calculate a Fourier difference map against the complex data set. One 3-nitropropionate (NPA) molecule and two 2-thenoyltrifluoroacetone (TTFA) molecules were clearly assigned with high contour level according to the omit map. Three important water molecules around the two TTFA inhibitors were added into the model. No further water molecules were picked for this low-resolution data set. This model with inhibitors was refined to a final R_{work} = 26.8% and R_{free} = 29.3%.

The data-collection, phase-calculation, and model-refinement statistics are summarized in Table 1.

Supplemental Data

Supplemental Data include Supplemental Experimental Procedures and four figures and are available with this article online at http://www.cell.com/cgi/content/full/121/7/1043/DC1/.

Acknowledgments

We are grateful to L. Wong, X.C. Zhang, and D. Xia for comments and critical discussion. We would also like to thank R. Zhang and A. Joachimiak (Advanced Photon Source, Argonne) for help with data collection and X. Zhang and X. Zhao for technical assistance. This work was supported by Project "973" (grant number 2004CB720000), Project "863" (grant number 2002BA711A12) and the NSFC (grant number 30221003).

Received: April 5, 2005
Revised: May 5, 2005
Accepted: May 19, 2005
Published: June 30, 2005

References

Abrahams, J.P., Leslie, A.G., Lutter, R., and Walker, J.E. (1994). Structure at 2.8 A resolution of F1-ATPase from bovine heart mitochondria. Nature *370*, 621–628.

Ackrell, B.A. (2002). Cytopathies involving mitochondrial complex II. Mol. Aspects Med. *23*, 369–384.

Astuti, D., Douglas, F., Lennard, T.W., Aligianis, I.A., Woodward, E.R., Evans, D.G., Eng, C., Latif, F., and Maher, E.R. (2001a). Germline SDHD mutation in familial phaeochromocytoma. Lancet *357*, 1181–1182.

Astuti, D., Latif, F., Dallol, A., Dahia, P.L., Douglas, F., George, E., Skoldberg, F., Husebye, E.S., Eng, C., and Maher, E.R. (2001b). Gene mutations in the succinate dehydrogenase subunit SDHB cause susceptibility to familial pheochromocytoma and to familial paraganglioma. Am. J. Hum. Genet. *69*, 49–54.

Bauters, C., Vantyghem, M.C., Leteurtre, E., Odou, M.F., Mouton, C., Porchet, N., Wemeau, J.L., Proye, C., and Pigny, P. (2003). Hereditary phaeochromocytomas and paragangliomas: a study of five susceptibility genes. J. Med. Genet. *40*, e75.

Baysal, B.E., Ferrell, R.E., Willett-Brozick, J.E., Lawrence, E.C., Myssiorek, D., Bosch, A., van der Mey, A., Taschner, P.E., Rubinstein, W.S., Myers, E.N., et al. (2000). Mutations in SDHD, a mitochondrial complex II gene, in hereditary paraganglioma. Science *287*, 848–851.

Baysal, B.E., Willett-Brozick, J.E., Lawrence, E.C., Drovdlic, C.M., Savul, S.A., McLeod, D.R., Yee, H.A., Brackmann, D.E., Slattery, W.H., 3rd, Myers, E.N., et al. (2002). Prevalence of SDHB, SDHC, and SDHD germline mutations in clinic patients with head and neck paragangliomas. J. Med. Genet. *39*, 178–183.

Birch-Machin, M.A., Taylor, R.W., Cochran, B., Ackrell, B.A., and Turnbull, D.M. (2000). Late-onset optic atrophy, ataxia, and myopathy associated with a mutation of a complex II gene. Ann. Neurol. *48*, 330–335.

Bourgeron, T., Rustin, P., Chretien, D., Birch-Machin, M., Bourgeois, M., Viegas-Pequignot, E., Munnich, A., and Rotig, A. (1995). Mutation of a nuclear succinate dehydrogenase gene results in mitochondrial respiratory chain deficiency. Nat. Genet. *11*, 144–149.

Brunger, A.T., Adams, P.D., Clore, G.M., DeLano, W.L., Gros, P., Grosse-Kunstleve, R.W., Jiang, J.S., Kuszewski, J., Nilges, M., Pannu, N.S., et al. (1998). Crystallography & NMR system: A new software suite for macromolecular structure determination. Acta Crystallogr. D Biol. Crystallogr. *54*, 905–921.

Douwes Dekker, P.B., Hogendoorn, P.C., Kuipers-Dijkshoorn, N., Prins, F.A., van Duinen, S.G., Taschner, P.E., van der Mey, A.G., and Cornelisse, C.J. (2003). SDHD mutations in head and neck paragangliomas result in destabilization of complex II in the mitochondrial respiratory chain with loss of enzymatic activity and abnormal mitochondrial morphology. J. Pathol. *201*, 480–486.

Esnouf, R.M. (1997). An extensively modified version of MolScript that includes greatly enhanced coloring capabilities. J. Mol. Graph. Model. *15*, 132–134, 112–113.

Gouet, P., Courcelle, E., Stuart, D.I., and Metoz, F. (1999). ESPript: analysis of multiple sequence alignments in PostScript. Bioinformatics *15*, 305–308.

Guo, J., and Lemire, B.D. (2003). The ubiquinone-binding site of the Saccharomyces cerevisiae succinate-ubiquinone oxidoreductase is a source of superoxide. J. Biol. Chem. *278*, 47629–47635.

Hagerhall, C. (1997). Succinate: quinone oxidoreductases. Variations on a conserved theme. Biochim. Biophys. Acta *1320*, 107–141.

Ingledew, W.J., Salerno, J.C., and Ohnishi, T. (1976). Studies on

electron paramagnetic resonance spectra manifested by a respiratory chain hydrogen carrier. Arch. Biochem. Biophys. *177*, 176–184.

Ishii, N., Fujii, M., Hartman, P.S., Tsuda, M., Yasuda, K., Senoo-Matsuda, N., Yanase, S., Ayusawa, D., and Suzuki, K. (1998). A mutation in succinate dehydrogenase cytochrome b causes oxidative stress and ageing in nematodes. Nature *394*, 694–697.

Iverson, T.M., Luna-Chavez, C., Cecchini, G., and Rees, D.C. (1999). Structure of the Escherichia coli fumarate reductase respiratory complex. Science *284*, 1961–1966.

Iwata, S., Lee, J.W., Okada, K., Lee, J.K., Iwata, M., Rasmussen, B., Link, T.A., Ramaswamy, S., and Jap, B.K. (1998). Complete structure of the 11-subunit bovine mitochondrial cytochrome bc1 complex. Science *281*, 64–71.

Jones, T.A., Zou, J.Y., Cowan, S.W., and Kjeldgaard, M. (1991). Improved methods for building protein models in electron density maps and the location of errors in these models. Acta Crystallogr. A *47*, 110–119.

Lancaster, C.R., Kroger, A., Auer, M., and Michel, H. (1999). Structure of fumarate reductase from Wolinella succinogenes at 2.2 A resolution. Nature *402*, 377–385.

Lange, C., and Hunte, C. (2002). Crystal structure of the yeast cytochrome bc1 complex with its bound substrate cytochrome c. Proc. Natl. Acad. Sci. USA *99*, 2800–2805.

Laskowski, R.A., MacArthur, M.W., Moss, D.S., and Thornton, J.M. (1993). PROCHECK: a program to check the stereochemical quality of protein structures. J. Appl. Crystallogr. *26*, 283–291.

Lee, G.Y., He, D.Y., Yu, L., and Yu, C.A. (1995). Identification of the ubiquinone-binding domain in QPs1 of succinate-ubiquinone reductase. J. Biol. Chem. *270*, 6193–6198.

Lemos, R.S., Fernandes, A.S., Pereira, M.M., Gomes, C.M., and Teixeira, M. (2002). Quinol:fumarate oxidoreductases and succinate:quinone oxidoreductases: phylogenetic relationships, metal centres and membrane attachment. Biochim. Biophys. Acta *1553*, 158–170.

Lu, G. (2000). A new method for Protein Structure Comparisons and Similarity Searches. J. Appl. Crystallogr. *33*, 176–183.

Maklashina, E., and Cecchini, G. (1999). Comparison of catalytic activity and inhibitors of quinone reactions of succinate dehydrogenase (Succinate-ubiquinone oxidoreductase) and fumarate reductase (Menaquinol-fumarate oxidoreductase) from Escherichia coli. Arch. Biochem. Biophys. *369*, 223–232.

Marti-Renom, M.A., Stuart, A.C., Fiser, A., Sanchez, R., Melo, F., and Sali, A. (2000). Comparative protein structure modeling of genes and genomes. Annu. Rev. Biophys. Biomol. Struct. *29*, 291–325.

Messner, K.R., and Imlay, J.A. (2002). Mechanism of superoxide and hydrogen peroxide formation by fumarate reductase, succinate dehydrogenase, and aspartate oxidase. J. Biol. Chem. *277*, 42563–42571.

Miki, T., Yu, L., and Yu, C.A. (1992). Characterization of ubisemiquinone radicals in succinate-ubiquinone reductase. Arch. Biochem. Biophys. *293*, 61–66.

Milunsky, J.M., Maher, T.A., Michels, V.V., and Milunsky, A. (2001). Novel mutations and the emergence of a common mutation in the SDHD gene causing familial paraganglioma. Am. J. Med. Genet. *100*, 311–314.

Neumann, H.P., Bausch, B., McWhinney, S.R., Bender, B.U., Gimm, O., Franke, G., Schipper, J., Klisch, J., Altehoefer, C., Zerres, K., et al. (2002). Germ-line mutations in nonsyndromic pheochromocytoma. N. Engl. J. Med. *346*, 1459–1466.

Niemann, S., and Muller, U. (2000). Mutations in SDHC cause autosomal dominant paraganglioma, type 3. Nat. Genet. *26*, 268–270.

Ohnishi, T., and Trumpower, B.L. (1980). Differential effects of antimycin on ubisemiquinone bound in different environments in isolated succinate. cytochrome c reductase complex. J. Biol. Chem. *255*, 3278–3284.

Otwinowski, Z., and Minor, W. (1997). Processing of X-ray diffraction data collected in oscillation mode. In Macromolecular Crystallography, Part A, C.W. Carter and R.M. Sweet, eds. (New York: Academic Press), pp. 307–326.

Oyedotun, K.S., and Lemire, B.D. (1999). The Saccharomyces cerevisiae succinate-ubiquinone oxidoreductase. Identification of Sdh3p amino acid residues involved in ubiquinone binding. J. Biol. Chem. *274*, 23956–23962.

Oyedotun, K.S., and Lemire, B.D. (2001). The Quinone-binding sites of the Saccharomyces cerevisiae succinate-ubiquinone oxidoreductase. J. Biol. Chem. *276*, 16936–16943.

Page, C.C., Moser, C.C., Chen, X., and Dutton, P.L. (1999). Natural engineering principles of electron tunnelling in biological oxidation-reduction. Nature *402*, 47–52.

Parfait, B., Chretien, D., Rotig, A., Marsac, C., Munnich, A., and Rustin, P. (2000). Compound heterozygous mutations in the flavoprotein gene of the respiratory chain complex II in a patient with Leigh syndrome. Hum. Genet. *106*, 236–243.

Rustin, P., and Rotig, A. (2002). Inborn errors of complex II—unusual human mitochondrial diseases. Biochim. Biophys. Acta *1553*, 117–122.

Ruzicka, F.J., Beinert, H., Schepler, K.L., Dunham, W.R., and Sands, R.H. (1975). Interaction of ubisemiquinone with a paramagnetic component in heart tissue. Proc. Natl. Acad. Sci. USA *72*, 2886–2890.

Salerno, J.C., Harmon, H.J., Blum, H., Leigh, J.S., and Ohnishi, T. (1977). A transmembrane quinone pair in the succinate dehydrogenase—cytochrome b region. FEBS Lett. *82*, 179–182.

Saraste, M. (1999). Oxidative phosphorylation at the fin de siecle. Science *283*, 1488–1493.

Shenoy, S.K., Yu, L., and Yu, C.A. (1997). The smallest membrane anchoring subunit (QPs3) of bovine heart mitochondrial succinate-ubiquinone reductase. Cloning, sequencing, topology, and Q-binding domain. J. Biol. Chem. *272*, 17867–17872.

Shenoy, S.K., Yu, L., and Yu, C. (1999). Identification of quinone-binding and heme-ligating residues of the smallest membrane-anchoring subunit (QPs3) of bovine heart mitochondrial succinate: ubiquinone reductase. J. Biol. Chem. *274*, 8717–8722.

Taschner, P.E., Jansen, J.C., Baysal, B.E., Bosch, A., Rosenberg, E.H., Brocker-Vriends, A.H., van Der Mey, A.G., van Ommen, G.J., Cornelisse, C.J., and Devilee, P. (2001). Nearly all hereditary paragangliomas in the Netherlands are caused by two founder mutations in the SDHD gene. Genes Chromosomes Cancer *31*, 274–281.

Terwilliger, T.C., and Berendzen, J. (1999). Automated MAD and MIR structure solution. Acta Crystallogr. D Biol. Crystallogr. *55*, 849–861.

Thompson, J.D., Higgins, D.G., and Gibson, T.J. (1994). CLUSTAL W: improving the sensitivity of progressive multiple sequence alignment through sequence weighting, position-specific gap penalties and weight matrix choice. Nucleic Acids Res. *22*, 4673–4680.

Tsukihara, T., Aoyama, H., Yamashita, E., Tomizaki, T., Yamaguchi, H., Shinzawa-Itoh, K., Nakashima, R., Yaono, R., and Yoshikawa, S. (1995). Structures of metal sites of oxidized bovine heart cytochrome c oxidase at 2.8 A. Science *269*, 1069–1074.

Tsukihara, T., Aoyama, H., Yamashita, E., Tomizaki, T., Yamaguchi, H., Shinzawa-Itoh, K., Nakashima, R., Yaono, R., and Yoshikawa, S. (1996). The whole structure of the 13-subunit oxidized cytochrome c oxidase at 2.8 A. Science *272*, 1136–1144.

Van Coster, R., Seneca, S., Smet, J., Van Hecke, R., Gerlo, E., Devreese, B., Van Beeumen, J., Leroy, J.G., De Meirleir, L., and Lissens, W. (2003). Homozygous Gly555Glu mutation in the nuclear-encoded 70 kDa flavoprotein gene causes instability of the respiratory chain complex II. Am. J. Med. Genet. A *120*, 13–18.

Xia, D., Yu, C.A., Kim, H., Xia, J.Z., Kachurin, A.M., Zhang, L., Yu, L., and Deisenhofer, J. (1997). Crystal structure of the cytochrome bc1 complex from bovine heart mitochondria. Science *277*, 60–66.

Xu, Y., Salerno, J.C., Wei, Y.H., and King, T.E. (1987). Stabilized ubisemiquinone in reconstituted succinate ubiquinone reductase. Biochem. Biophys. Res. Commun. *144*, 315–322.

Yankovskaya, V., Sablin, S.O., Ramsay, R.R., Singer, T.P., Ackrell, B.A., Cecchini, G., and Miyoshi, H. (1996). Inhibitor probes of the

quinone binding sites of mammalian complex II and Escherichia coli fumarate reductase. J. Biol. Chem. *271*, 21020–21024.

Yankovskaya, V., Horsefield, R., Tornroth, S., Luna-Chavez, C., Miyoshi, H., Leger, C., Byrne, B., Cecchini, G., and Iwata, S. (2003). Architecture of succinate dehydrogenase and reactive oxygen species generation. Science *299*, 700–704.

Yu, L., Xu, J.X., Haley, P.E., and Yu, C.A. (1987). Properties of bovine heart mitochondrial cytochrome b560. J. Biol. Chem. *262*, 1137–1143.

Zhang, Z., Huang, L., Shulmeister, V.M., Chi, Y.I., Kim, K.K., Hung, L.W., Crofts, A.R., Berry, E.A., and Kim, S.H. (1998). Electron transfer by domain movement in cytochrome bc1. Nature *392*, 677–684.

Accession Numbers

The coordinates and structure factors for the wild-type Complex II structure have been deposited in the Protein Data Bank with ID code 1ZOY. The coordinates and structure factors for the Complex II structure bound with inhibitors have been deposited in the Protein Data Bank with ID code 1ZP0.